J. Am. Ceram. Soc., 94 [2] 367–371 (2011)
DOI: 10.1111/j.1551-2916.2010.04343.x

journal

A Foaming Esterification Sol–Gel Route for the Synthesis of Magnesia–Yttria Nanocomposites

Chun-Hu Chen,[‡] Jacquelynn K. M. Garofano,[§] Chigozie K. Muoto,[§] Andrew L. Mercado,[‡] Steven L. Suib,[‡] Mark Aindow,[§] Maurice Gell,[*,§] and Eric H. Jordan[*,†,¶]

[‡]Department of Chemistry, Institute of Materials Science, University of Connecticut, Storrs, Connecticut 06269

[§]Department of Chemical, Materials and Biomolecular Engineering, Institute of Materials Science, University of Connecticut, Storrs, Connecticut 06269

[¶]Department of Mechanical Engineering, Institute of Materials Science, University of Connecticut, Storrs, Connecticut 06269

Nanocomposites of MgO with Y_2O_3 have been produced from the respective nitrates by an esterification reaction with ethylene glycol and citric acid. The evolution of nitrous oxides during the reaction causes the product to foam, and the calcination of this foam gives nanocomposite powders with extremely fine, uniform grains, and phase domains. These microstructures are remarkably stable both under postcalcination heat treatment and during consolidation by hot pressing. These stable microstructures arise as a result of the decomposition sequence: this involves the formation of a metastable amorphous/vitreous intermediate followed by concurrent crystallization and phase separation on the nanoscale.

I. Introduction

THERE are two main reasons for the recent interest in nanocomposite ceramics. Firstly, these materials can exhibit enhanced properties as compared with the corresponding coarse-grained ceramic composites or with single-phase nanostructured ceramics.[1–6] The range of properties that can be influenced by the structure of nanocomposite ceramics include the mechanical, chemical, thermal, electrical, magnetic, and optical responses.[7–12] Secondly, nanocomposite ceramics can exhibit greatly enhanced microstructural stability as compared with single-phase nanostructured ceramics, which is particularly important for materials that will experience high temperatures during processing and/or service.[13] This microstructural stability arises due to grain-boundary pinning and/or lower coarsening rates for phase domains than for grains within a domain: both effects are enhanced in nanocomposites with fine, uniformly-dispersed phase domains.[14]

The production of nanocomposite ceramics with fine uniform phase domains is particularly challenging due to the need to control both the microstructural length scales and the elemental distributions.[15] Many of the conventional synthetic methods for producing ceramics (e.g., precipitation, hydrothermal, reflux, thermal decomposition, etc.) are not amenable to such control because of the reaction/nucleation rates involved and/or the physical/chemical properties of the components. Although various different approaches have been developed to overcome these limitations[16] these typically involve complex equipment, extremely high temperatures and/or low yields, resulting in high production cost.

Sol–gel methods utilize lower temperatures and offer a greater degree of control over elemental ratios and homogeneity than most of the methods mentioned above.[17] The main drawback is that effective sol–gel processing requires precise control of synthesis conditions and expensive organometallic precursors. Thus, sol–gel processed nanocomposite ceramics can also be expensive. A less costly derivative of the sol–gel technique is esterification sol–gel (ESG) processing, which utilizes esterification of less expensive precursors to create a similar sol–gel environment under a wider range of synthesis conditions.[18,19] This ESG approach has been used recently for the synthesis of catalytic nanoparticles and metal oxide/polymer nanocomposites, but to our knowledge the only previous report on synthesis of oxide/oxide composites via this route is by Jiang and Mukherjee.[20] In their study chloride precursors were used to produce magnesia–yttria ($MgO–Y_2O_3$) nanocomposites via an ESG process, but no microstructural details were reported.

This study is part of a program concerning the synthesis of oxide/oxide nanocomposites for optical applications. The motivation for this work is the reduction in optical scattering at phase boundaries when the phase domains are smaller than the wavelength of the electromagnetic photons.[21] Homogeneously distributed submicrometer phase domains have been obtained in $MgO–ZrO_2$[22] and $MgO–Y_2O_3$[23] composites processed using a combined sol–gel/thermal decomposition route. Here we describe a foaming ESG method for the synthesis of nanocomposite $MgO–Y_2O_3$ powders. This approach results in nanocrystalline powders with fine, homogeneously-distributed phase domains, and these powders can be consolidated by vacuum hot-pressing while retaining a uniform nanoscale phase domain structure. This simple inexpensive approach could be extended to a wide variety of nanocomposite ceramic systems, thereby making the use of such materials a viable proposition in a range of different applications.

II. Experimental Procedure

$MgO–Y_2O_3$ composites were prepared via an ESG route using the following reagents: magnesium nitrate ($Mg(NO_3)_2 \cdot 6H_2O$), yttrium nitrate ($Y(NO_3)_3 \cdot 6H_2O$), citric acid, and 99.0% ethylene glycol (Alfa Aesar, Ward Hill, MA). Several different composite compositions were produced from these reagents, but for

M. Cinibulk—contributing editor

Manuscript No. 28723. Received October 5, 2010; approved November 16, 2010.
This work was supported by Raytheon Company as part of a DARPA-sponsored ONR project.
*Member, The American Ceramic Society.
†Author to whom correspondence should be addressed. e-mail: jordan@engr.uconn.edu

Fig. 1. Foam products from the esterification sol–gel synthesis: (a) as-synthesized organic foam, and (b) oxide composite foam produced by calcining the sample from (a) in air at 400°C for 24 h.

brevity we present here only data from the reagent mixture that resulted in composites with approximately 90 mol% MgO. Two aqueous solutions of 0.5M $Y(NO_3)_3$ and 0.5M $Mg(NO_3)_2$ were prepared first using distilled deionized (DDI) water. In a typical synthesis 7.68 g of citric acid (40 mmol) was dissolved in 80 mL of DDI water in a 600 mL beaker and then 0.826 g of ethylene glycol (13 mmol) was added yielding a clear and colorless solution. After stir aging for 5 min, 14 mL of 0.5M $Y(NO_3)_3$ (7 mmol) and 66 mL of 0.5M $Mg(NO_3)_2$ (33 mmol) were added sequentially into the clear organic solution. After another 10 min of stirring, the beaker containing the solution was placed into an oven preheated to 200°C. This stage of the process promotes the esterification reaction since decomposition of citric acid occurs at $\approx$170°C. Upon removal from the oven after 3 h the beaker was filled completely with highly porous pale-brown foam (Fig. 1(a)). The form of this product is consistent with the generation of nitrous oxides (NO_x) during the esterification reaction between citric acid and glycol, resulting in a porous organic foam. The brown color of the foam indicates that there are carbonaceous species in the material, presumably due to the onset of decomposition in the polymerized network. The presence of carbonates was confirmed in separate Fourier transform-infrared (FTIR) spectroscopy experiments.

The material was then calcined at 400°C for 24 h in a muffle furnace to convert the Mg- and Y-containing organic foam to the oxide composite. This results in significant volume shrinkage and a change in color to pure white (Fig. 1(b)), indicating the removal of the C (here again confirmed by FTIR spectroscopy). To evaluate the microstructural development/stability in the composite material, samples of the white foam were crushed to powder form and then subjected to postcalcination heat-treatment (PCHT) for 1 h at 800° and 1100°C. Preliminary consolidation trials were performed by: pulverizing the calcined (400°C) foam in a SPEX mill; introducing 6 g of the powder into a vacuum hot press; evacuating the chamber to a background pressure of 66 mPa; heating the chamber to 900°C and allowing the powder to out-gas for 30 min; applying an axial pressure of 20 MPa; heating gradually (over 90 min) to 1300°C and maintaining the axial pressure for 30 min; and then unloading and cooling to ambient temperature under vacuum in the chamber. As a basis for comparison, an additional powder sample was prepared with a PCHT of 30 min at 1300°C to mimic the final stage of the hot-pressing sequence.

The structural characteristics of the composite materials were evaluated by a combination of: X-ray diffractometry (XRD; XDS-2000, Scintag Inc., Cupertino, CA); scanning electron microscopy (SEM; TM-1000, Hitachi, Tokyo, Japan); transmission electron microscopy (TEM, FEI Tecnai T12, FEI Company, Hillsboro, OR), and sectioning in a dual-beam focused ion beam (FIB)/SEM (FEI Strata 400S, FEI Company, Hillsboro, OR). All of the latter three instruments are equipped with energy-dispersive X-ray spectrometers (EDXS), which were used to measure local chemistry. Powdered foam samples were prepared for TEM by dispersing the flakes onto a copper mesh grid coated with a holey carbon film (Quantifoil Micro Tools GmbH, Jena, Germany). Difficulties were experienced in preparing thin TEM specimens from the consolidated material and so the microstructure was evaluated using back-scattered electron (BSE) SEM images obtained from FIB-cut sections. Measurements of grain sizes were obtained from the SEM and TEM images using the mean linear intercept method.

III. Results

The morphology of the oxide composite after calcining (400°C, 24 h) is revealed clearly in secondary electron SEM images such as those shown in Fig. 2. Figure 2(a) is a low-magnification image showing the cellular structure of the as-calcined foam, and Fig. 2(b) is a higher-magnification detail of the powder obtained by crushing this foam. The flakes in the latter image are up to 0.5 μm in thickness and these correspond to fragments of the cell walls from the calcined foam.

The phases present in the oxide composites were confirmed by XRD and examples of the spectra obtained are shown in Fig. 3 for: (a) the as-calcined (400°C, 24 h) powder sample; (b) and (c) the powders subjected to PCHTs at 800° and 1100°C, respec-

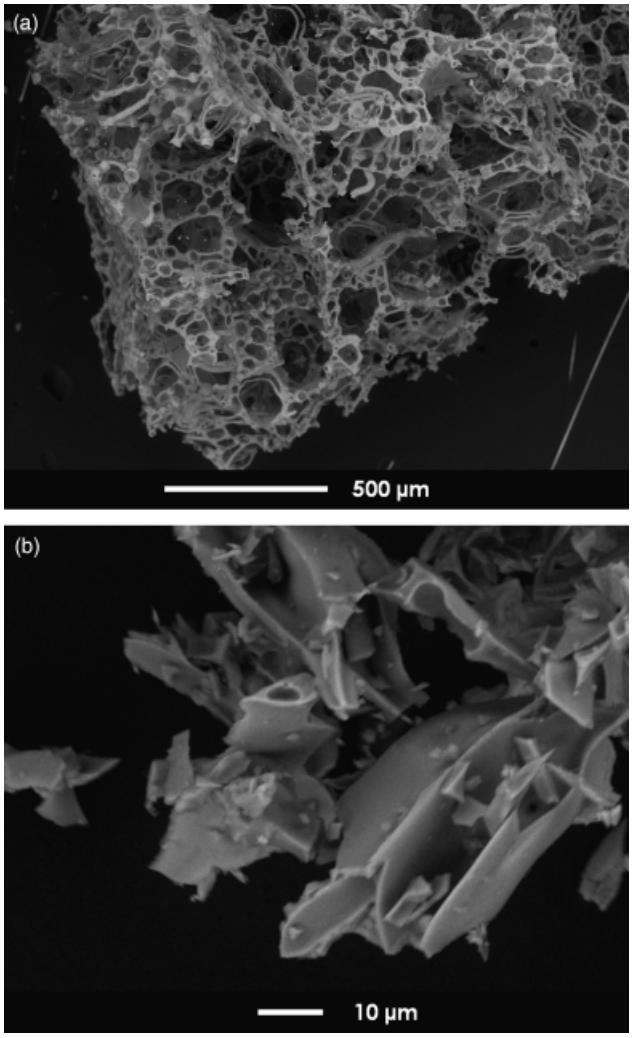

Fig. 2. Secondary electron SEM image obtained from the oxide composite sample shown in Fig. 1(b): (a) low-magnification view showing the morphology of the cells in the as-calcined (400°C, 24 h) foam; (b) higher magnification view of flake-like powder particles produced by crushing the foam shown in (a).

tively; and (d) the sample consolidated by hot-pressing at 1300°C. The as-calcined sample gives a high diffuse background with three broad peaks corresponding to cubic MgO (200, 220, and 222) and only a single, very broad 222 cubic Y_2O_3 peak:

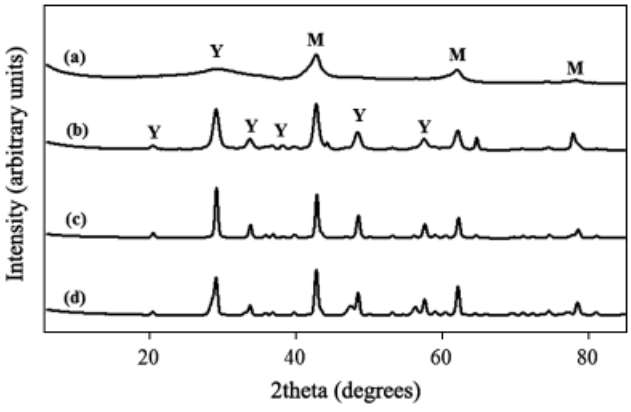

Fig. 3. XRD spectra obtained from the MgO–Y_2O_3 nanocomposite materials: (a) as-calcined (400°C, 24 h); (b) after PCHT for 1 h at 800°C; (c) after PCHT for 1 h at 1100°C; and (d) sample consolidated by vacuum hot pressing at 1300°C. M, cubic MgO peaks (JCPDS: 04–829); Y, cubic Y_2O_3 peaks (JCPDS: 41–1105).

these data indicate that the sample consists of a mixture of extremely fine grains and amorphous material. In contrast, the PCHT and consolidated samples give no diffuse background, all of the peaks expected for cubic magnesia and yttria, and much narrower peaks. This indicates that the samples are fully crystalline with somewhat larger grain sizes. There are some differences in the relative intensities of the peaks between the PCHT and consolidated samples. Since the XRD data were acquired from the surface of the consolidated sample because of difficulties experienced in crushing this material to powder form, the differences in peak intensities presumably arise because of crystallographic texture that develops during hot pressing.

Further details on the grain and phase domain sizes were obtained by TEM. The microstructures were found to be remarkably uniform from region to region within a flake and from flake to flake for a particular sample. Examples of typical bright field (BF) TEM images with selected area diffraction patterns (SADPs) inset are shown in Figs. 4(a)–(c) for: the as-calcined (400°C, 24 h) powder sample and the powders subjected to PCHTs for 1 h at 800°C and 1 h at 1100°C, respectively. In each case the EDXS data (not shown here) were consistent with the nominal composition. The as-calcined powder (Fig. 4(a)) is comprised of very fine crystallites (< 10 nm in diameter) embedded in an amorphous matrix, as-expected from the XRD data, and most of the rings in the SADPs correspond to MgO indicating that the amorphous phase is probably rich in Y_2O_3. For the sample subjected to PCHT at 800°C (Fig. 4(b)), the grains were up to 30 nm in diameter and there was no evidence of residual amorphous phase. The magnesia and yttria grains were identified by use of tilting experiments to distinguish mass-thickness from diffraction contrast, and the mean grain sizes for MgO and Y_2O_3 were 24 and 14 nm, respectively. More significant coarsening was evident in the sample subjected to PCHT at 1100°C (Fig. 4(c)) with grains of up to 80 nm in diameter giving "spottier" rings in the SADPs. In this case the mass-thickness contrast was more pronounced (Y_2O_3 grains appear dark) and here again the MgO grains are coarser than those of Y_2O_3 with mean diameters of 65 and 42 nm, respectively. We note that cubic MgO and Y_2O_3 are the only crystalline phases detected. Figure 4(d) is an enlargement of half of the inset to Fig. 4(b) with the four most intense rings for each phase indexed; all of the weaker rings also correspond to those expected for these phases.

The sample consolidated by hot pressing at 1300°C had an Archimedes' density of 96.6%, indicating that the flake-like composite powder can be sintered readily. An example of a BSE SEM image obtained from a FIB-cut section through the consolidated sample is shown in Fig. 5(a). Compositional contrast dominates such images with the Y_2O_3 appearing bright and the MgO dark (i.e., the opposite of that for BF TEM images). The phase domains in this sample are up to 500 nm in diameter and the largest MgO grains are around 300 nm in diameter. A representative BF TEM image obtained from the powder sample with a PCHT of 30 min at 1300°C is shown in Fig. 5(b), and the sizes and morphologies of the grains and phase domains are remarkably similar to those in Fig. 5(a).

IV. Discussion

The microstructural observations presented here demonstrate that the foaming ESG method can be used to produce oxide nanocomposites with fine, homogenously distributed grains, and phase domains. We ascribe the scale and uniformity of the microstructure to the way in which the organic foam decomposes to form the oxide composite. The organic product of the esterification reaction will contain an intimate mixture of the Mg^{2+} and Y^{3+} cations, and thus the scale of the composite microstructure formed during calcination will be dictated by the way in which phase separation occurs. The organic product of the reaction is a foam with thin walls, so we would expect de-

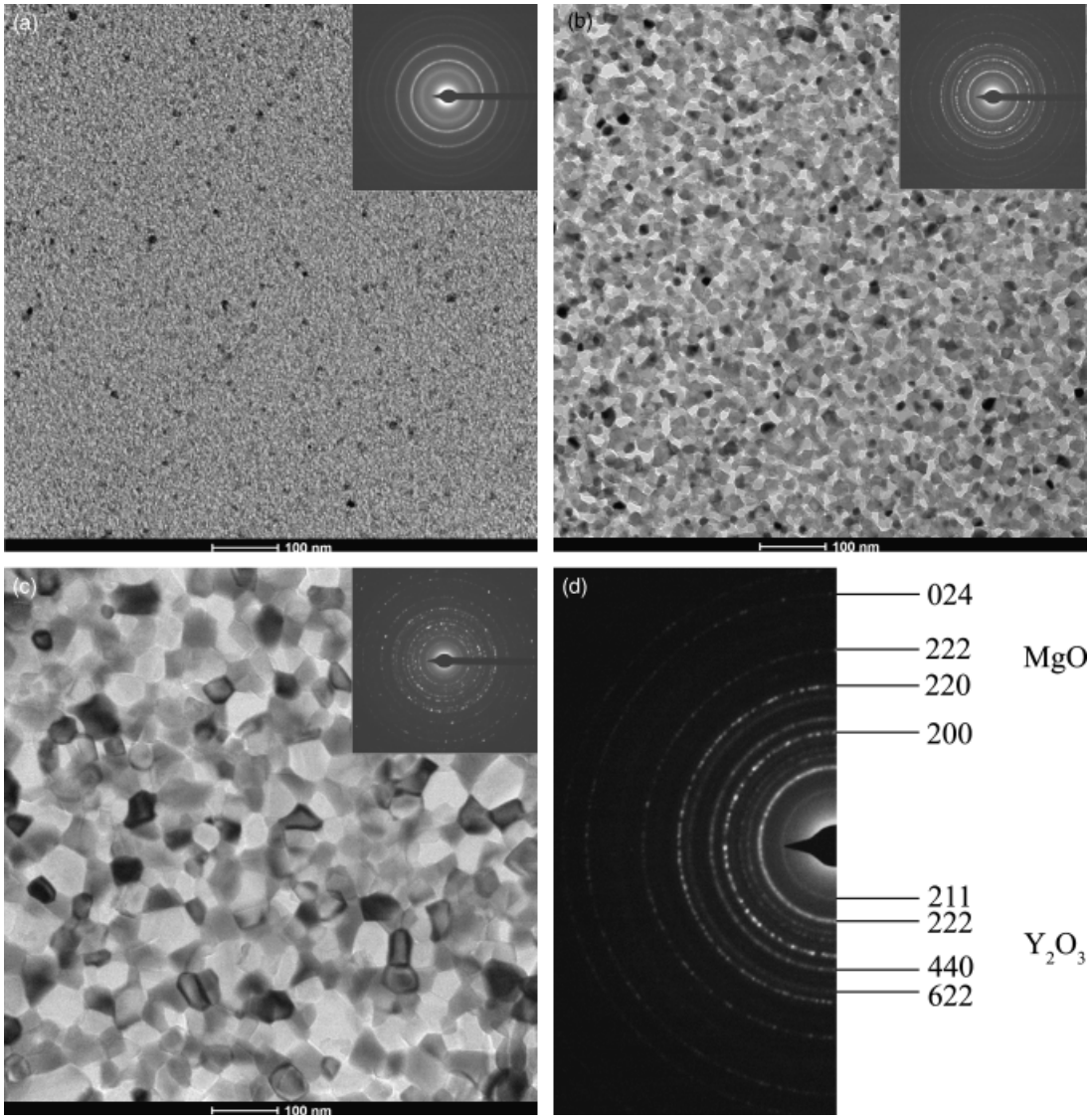

Fig. 4. (a–c) Representative BF TEM images with inset SADPs obtained from flakes of the oxide nanocomposites: (a) as-calcined (400°C, 24 h); (b) after PCHT for 1 h at 800°C; (c) after PCHT for 1 h at 1100°C. For the fully crystalline samples in (b) and (c) the darkest grains are Y_2O_3 and the lightest grains are MgO due to mass-thickness contrast; intermediate levels of intensity are observed due to diffraction contrast effects and in these cases tilting experiments are required to distinguish Y_2O_3 from MgO. (d) enlarged view of the inset SADP in (b) showing the indices for the four most intense rings from each phase.

composition during calcination to occur more rapidly and more homogeneously than for a dense solid product. Since the XRD and TEM data from the calcined sample show significant amorphous material, it is reasonable to assume that the decomposition proceeds firstly by the formation of a homogeneous vitreous mixed oxide, and that phase separation then occurs by the nucleation and growth of the constituent crystalline oxides. Thus, since MgO and Y_2O_3 have only very limited mutual solid solubility, the length scale of the phase domains formed during crystallization will be dictated by mass transport of Mg and Y, which will be very slow at the calcination temperature of 400°C.

As discussed previously,[23] since there is no possibility of forming a homogeneous crystalline solid solution at elevated temperatures, the phase domain distribution established in the oxides during calcination will not change dramatically during PCHT. The grains in a given phase domain may coalescence to form larger grains because only short-range atomic movements are required, but the interphase boundaries will be relatively immobile because phase domain growth involves longer-range mass transport. This is presumably the reason for the remarkable stability of the composite microstructure, with the retention of nanoscale grains/phase domains even after PCHT or hot pressing at temperatures as high as 1300°C. The initial low-temperature calcination step is critical to produce the intermediate amorphous/vitreous state and thus to establish this stable phase distribution. In separate trials performed by heating the organic foam to 800° or 1100°C directly without the initial calcination, the same MgO and Y_2O_3 phases were formed but the grain and phase domain sizes were larger and less uniform.

V. Summary

Stable homogeneous MgO–Y_2O_3 nanocomposites with fine grains and phase domains have been produced successfully by using a novel foaming ESG procedure. This process utilizes inexpensive precursors and mild conditions to form a low-density homogeneous organic foam. The conversion of this foam to the required oxides is achieved by a low-temperature calcination followed by higher-temperature postcalcination heat treatment. The formation of a metastable amorphous intermediate during the calcination is critical to establishing a fine, homogeneous, stable phase domain structure. This simple inexpensive procedure could be modified easily for the production of other oxide/oxide composites.

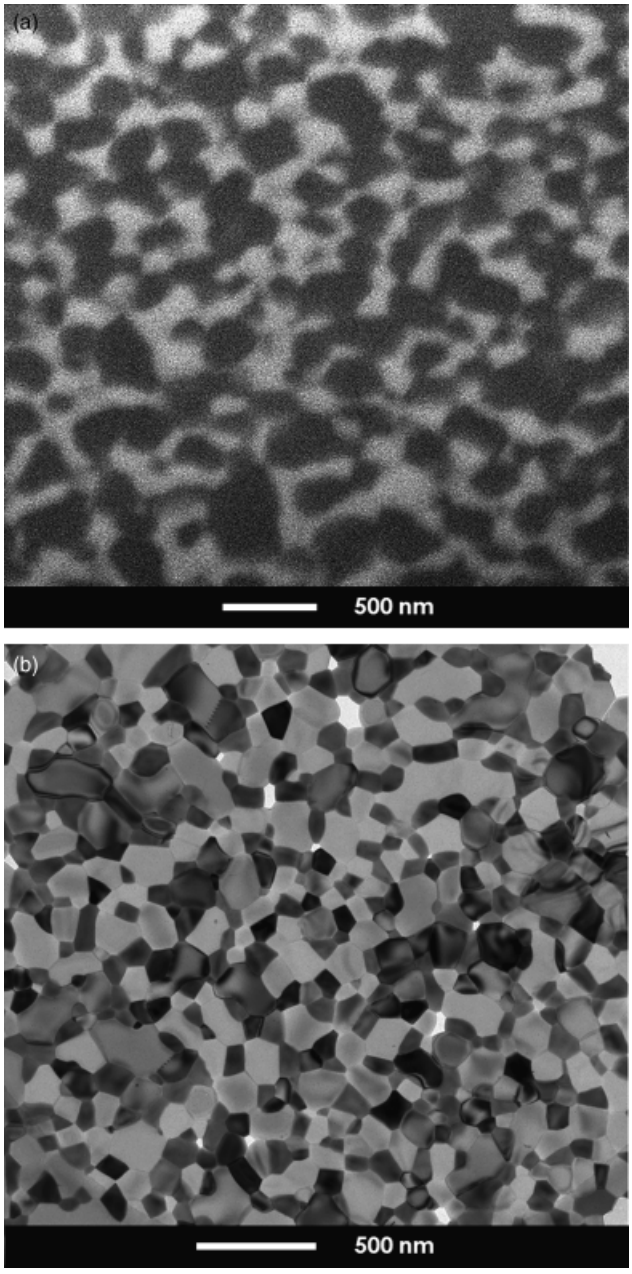

Fig. 5. Comparison of grain and phase domain sizes in: (a) the sample consolidated by vacuum hot pressing at 1300°C (BSE SEM image from a FIB-cut section—bright regions are Y_2O_3, dark regions are MgO); and (b) powder subjected to PCHT for 30 min at 1300°C (BF TEM image—contrast as for Figs. 4(a)–(c)).

References

[1]I. R. Abothu, P. Poosanaas, S. Komarneni, Y. Ito, and K. Uchino, "Nanocomposite Versus Monophasic Sol–Gel Processing of PLZT Ceramics," *Ferroelectrics*, **231**, 187–92 (1999).

[2]M. Gell, "Applying Nanostructured Materials to Future Gas Turbine Engines," *JOM*, **46**, 30–4 (1994).

[3]H. Gleiter, "Nanostructured Materials: Basic Concepts and Microstructure," *Acta Mater.*, **48**, 1–29 (2000).

[4]R. W. Siegel, "Nanostructured Materials—Mind Over Matter," *Nanostruct. Mater.*, **3**, 1–18 (1993).

[5]Y. Yamazaki, H. Gleiter, K. Lu, Z. Ou-Yang, and X. Zhu, "Mesoscopic Phase Transition of Nanostructured Materials: Construction of Computer Experimental Systems, Synthesis and Control of Functional Properties," *Surf. Interface Anal.*, **36**, 177–83 (2004).

[6]J. Karthikeyan, C. C. Berndt, S. Reddy, J. Wang, A. H. King, and H. Herman, "Nanomaterial Deposits Formed by DC Plasma Spraying of Liquid Feedstocks," *J. Am. Ceram. Soc.*, **81**, 121–8 (1998).

[7]Z. Cui and H. Hahn, "Tensile Deformation of Nanostructured TiO_2 at Low Temperatures," *Nanostruct. Mater.*, **1**, 419–25 (1992).

[8]R. W. Rice, "Ceramic Tensile Strength-Grain Size Relations: Grain Sizes, Slopes, and Branch Intersections," *J. Mater. Sci.*, **32**, 1673–92 (1997).

[9]H. Hahn and R. S. Averback, "High Temperature Mechanical Properties of Nanostructured Ceramics," *Nanostruct. Mater.*, **1**, 95–100 (1992).

[10]R. S. Averback, H.J Höfler, H. Hahn, and J. C. Logas, "Sintering and Grain Growth in Nanocrystalline Ceramics," *Nanostruct. Mater.*, **1**, 173–8 (1992).

[11]T. Stefanik, R. Gentilman, and P. Hogan, "Nanocomposite Optical Ceramics for Infrared Windows and Domes"; pp. 65450A1–5 *Proceedings of SPIE - International Society. for Optical Engineer*, Orlando, FL, 2007.

[12]C. S. Nordahl, T. Hartnett, T. Gattuso, R. Gentilman, and J. McCloy, "Mechanical, Optical & Thermal Properties of Nano-Composite Optical Ceramics pp. 1–6 in *Proceedings of the 12th DoD Electromagnetic Windows Symposium,* Redstone Arsenal, AL, 2008

[13]B. H. Kear and W. E. Mayo, "On the Processing of Nanostructured Ceramics," *Mater. Sci. Forum*, **437–438**, 399–402 (2003).

[14]F. F. Lange, M. L. Balmer, and C. G. Levi, "Diffusion Limited Crystallization and Phase Partitioning in ZrO_2-Metal Oxide Binary Systems – Code: D3," *J. Sol–Gel Sci. Technol.*, **2**, 317–21 (1994).

[15]G. A. Chow and K. E. Gonsalves, "Particle Synthesis by Chemical Routes"; pp. 55–7 in *Nanomaterials: Synthesis Properties and Applications*, Edited by A. S. Edelstein and R. C. Cammarata. Taylor & Francis Group, New York, 1996.

[16]J. Azurdia, J. Marchal, and R. M. Laine, "Synthesis and Characterization of Mixed-Metal Oxide Nanopowders Along the CoO_x–Al_2O_3 Tie Line Using Liquid-Feed Flame Spray Pyrolysis," *J. Am. Ceram. Soc.*, **89**, 2749–56 (2006).

[17]L. L. Hench and J. K. West, "The Sol–Gel Process," *Chem. Revs.*, **90**, 33–72 (1990).

[18]A. Kareiva, I. Bryntse, M. Karppinen, and L. Niinisto, "Influence of Complexing Agents on Properties of $YBa_2Cu_4O_8$ Superconductors Prepared by the Sol–Gel Method," *J. Solid State Chem.*, **121**, 356–61 (1996).

[19]M. Veith, S. Mathur, A. Kareiva, M. Jilavi, M. Zimmer, and V. Huch, "Low Temperature Synthesis of Nanocrystalline $Y_3Al_5O_{12}$ (YAG) and Ce-Doped $Y_3Al_5O_{12}$ via Different Sol–Gel Methods," *J. Mater. Chem.*, **9**, 3069–79 (1999).

[20]D. T. Jiang and A. K. Mukherjee, "Synthesis of Y_2O_3–MgO Nanopowder and Infrared Transmission of the Sintered Nanocomposite"; pp. 703007A1–5 *Proceedings of SPIE - International Society for Optical Engineer*, San Diego, CA, 2008.

[21]D. T. Jiang and A. K. Mukherjee, "Spark Plasma Sintering of an Infrared-Transparent Y_2O_3–MgO Nanocomposite," *J. Am. Ceram. Soc.*, **93**, 769–73 (2010).

[22]C. K. Muoto, E. H. Jordan, M. Gell, and M. Aindow, "Phase Homogeneity in Sol–Gel/Combustion Synthesized MgO–ZrO_2 Nano Composites," *J. Am. Ceram. Soc.*, **93**, 3102–9 (2010).

[23]C. K. Muoto, E. H. Jordan, M. Gell, and M. Aindow, "Effects of Precursor Chemistry on the Structural Characteristics of Sol–Gel/Combustion Synthesized Y_2O_3–MgO Nanocomposites," *J Am. Ceram. Soc.* doi: 10.1111/j.1551-2916.2010.04078.x. □